

**Mineralogical and geochemical variation in hydrothermal sulfides from Vienna Woods field, Manus Basin, Papua New Guinea: Constraints on their evolution**

**Durbar Ray<sup>1\*</sup>, Ranadip Banerjee<sup>1</sup>, Aninda Mazumder<sup>1</sup>, Anil L. Paropkari<sup>1</sup>,  
Subir Mukhopadhyay<sup>2</sup>, S. Balakrishnan<sup>3</sup>**

<sup>1</sup> CSIR-National Institute of Oceanography, Dona Paula, Goa-403004, India.

<sup>2</sup> Department of Geological Sciences, Jadavpur University, Kolkata-700032, India.

<sup>3</sup> Department of Earth Sciences, Pondicherry University, Puducherry-605014, India.

\*Corresponding author: Durbar Ray, CSIR-National Institute of Oceanography, Goa-403004.

Email: dray@nio.org, Phone no. +91-832-2450478; Fax no. +91-832-2450602

**Abstract**

Polymetallic sulfides from two hydrothermal chimneys and talus deposit from the Vienna Woods field of Manus Basin were studied for mineralogy, elemental composition, and S-isotope ratio to understand their evolution. The factors including nature of source fluid, mineral paragenesis, and related geochemical processes have been discussed. Mineralogy and elemental concentration of Cu and Fe-rich large chimney at the central part of this hydrothermal field was completely different from the smaller Zn-rich peripheral chimney and Fe-rich talus deposit; suggesting the variable degree of alterations generate physio-chemically different source fluids responsible for these hydrothermal structures. Similarly, S-isotope ratios also indicate chemically diverse fluids and different modes of precipitation were involved in their evolution. Distinct mineral zonings and associated elemental and isotopic compositions within individual deposit confirm paragenetic shifts were involved during their growth process.

**Key words:** Manus Basin, hydrothermal chimney, talus, geochemistry, mineralogy.

## **1. Introduction**

The western part of the Pacific plate has a number of convergent segments, marking the boundaries of more than 75 % marginal basins found on the earth today (Tamaki and Honza, 1991). Some of these marginal basins developed due to seafloor spreading behind the magmatic arcs and are well known for seafloor hydrothermal activities. Over the last two decades several explorations in these marginal basins have shown that this region has wide variation in hydrothermal activities and associated ore deposits (Ishibashi and Urabe, 1995). In the Manus Basin, evidence of hydrothermal activity was first recorded in 1985 -86 with deep tow camera which photographed a variety of vent fauna within the Manus Spreading Center (Both 1986). Later, many active and extinct hydrothermal fields (e.g. Vienna Woods, Solwara, PACMANUS, NE Pual, DESMOS and SuSu Knoll) were found at different parts of this basin (Tufer et al., 1990; Auzende et al., 1996; 2000; Lisitsyn et al., 1997; Sinton 1997). Several authors described the nature of hydrothermal deposits of these vent fields, based on bulk mineralogy and geochemistry (Tufar, 1990; Lisitsyn et al., 1993; Lein et al., 1993; Binns and Scott 1993; Kim et al., 2004). In the present study, the evolutionary histories of three different hydrothermal deposits have been discussed based on the small-scale variations of minerals, elemental composition and sulfur isotopic ratios. The chemical characterization of different mineral zonings across the section of individual sulfide structure has provided better insights about mineral paragenesis at different growth phases of these deposits.

## **2. Local geological settings**

At the northeast of Papua New Guinea, the Manus Basin has a complex tectonic setting; bounded by inactive Manus Trench in the north and active New Britain Trench in the south (Binns and Scott 1993). In the northeastern part of the Bismarck Sea, this basin represents a typical back-arc setting with respect to New Britain volcanic arc-trench system (Fig. 1). Within this marginal basin relative motion between the Pacific plate and the Bismarck plate occurs along three NW-SE trending lateral transform faults (i.e., Willaumez, Djaul and Weitin Faults) and four spreading segments (i.e., Southeast Rift; Southern Rift; Manus Spreading Center and Extensional Transform Zone) offset by those faults (Martinez and Taylor 1996). In the central part of the Manus Basin 120 km long Manus Spreading Center (MSC in Fig. 1) is a well developed spreading axis located between Willaumez transform fault (3°42'S, 149°37'E) and Djaul transform fault (3°S, 150°34'E) (Reeves et al., 2011). The estimated spreading rate of MSC varies from zero to 9.2 cm/yr. The

variable spreading rate made it wide (~ 72 km) and shallow at the southwest end and narrowed down to almost zero at the deeper northeastern tip (Taylor et al., 1994; Martinez and Taylor, 1996). Studies showed that transitional mid-oceanic ridge basalt (T-MORB) was mostly present within the rift valley (Lizitsyn et al., 1993; Mudholkar and Paropkari, 1999; Sinton et al., 2003). In the southernmost end of the spreading axis, occurrence of back-arc basin basalt (BABB) also has been reported (Tufar, 1990; Sinton et al., 2003). The valley floor of MSC hosts for two active hydrothermal fields (e.g. Vienna Woods and Worm Garden; Fig. 1) at the water depths of ~2470 m. The Vienna Woods field on an axial graben near 03°09.75'S, 150°16.83'E, at the northern part of the valley, is a large vent field having diameter more than 300 m (Auzende et al., 1996).

### **3. Materials and Methods**

During 21<sup>st</sup> cruise of *R/V Akademik Mstislav Keldysh* (May–June, 1990), the Vienna Woods hydrothermal field has been explored thoroughly with “MIR” manned submersibles (Lizitsyn et al., 1993; 1997). Sulfide samples from two chimneys of different heights and talus deposit (Table 1) from that vent field, collected during that cruise, has been used for the present study.

#### ***3.1. Detailed description of sample and sub-sampling***

During underwater observation with MIR manned submersible (dive #M2255), three closely spaced clusters of hydrothermal chimneys were found within the Vienna Woods field (Tufar, 1990; Lein et al., 1993). In this vent field sheet-like sulfide base was found to host tubular chimneys of variable heights (2-14 m; Fig. 2A) (Lein et al., 1993; Lizitsyn et al., 1993; Reeves et al., 2011). The sample, M2255-2 (Fig. 2B) is a horizontal section of a small (~4.0 m) active chimney, located on the outer edge of that sulfide base. The hand-specimen of this chimney section has distinct colored layers from outer rim to the inner orifice and three sub-samples were made mostly based on color variation. The dark black layer around the chimney orifice (O2) was carefully separated from the brown colored middle layer (M2) and exterior rim with several white patches (E2) (Fig. 2B). Another chimney sample, M2255-10 was obtained from a large active gray smoker (height 14 m and basal diameter >5.0 m), located at the central part of the same chimney cluster (Fig. 2A). The hand specimen in Fig. 2C represents a vertical section from the top most part of a side projection of that giant columnar chimney. This section has a central fluid conduit which was dark in color relative to lateral portions on either side. Three sub-sections (L10, C10, and R10) were made based on the position of the tortuous fluid channel as shown in Fig. 2C. The third sample, M2255-9

shows a vertical section of sulfide talus accumulated at the base of the central chimney (Fig. 2A). This talus section of height 15 -20 cm has more or less uniform appearance and sub-sampled into four concentric sections as shown in Fig. 2D. The section, P9 represents the porous surface layer of the talus while T9, C9 and B9 correspond to the top, central and bottom layers of the same deposit. All these sub-samples from each hydrothermal structure were analyzed separately for mineralogy, major and trace element composition and S-isotope ratio.

### ***3.2. Mineralogy***

Mineralogy of fine powders of each sub-sample was analyzed with an X-ray diffractometer (Model: Philips PW-1840) by using Cu-K $\alpha$  radiation over the  $2\theta$  range from  $05^\circ$  to  $60^\circ$ . For textural investigation of minerals, small chips of each sub-sample and polished section of selective samples were scanned with a Scanning Electron Microscope (JEOL JSM-5410LV). An Energy-dispersive X-ray Spectrometer attached to SEM was used for qualitative chemical analysis. All these analyses were carried out at CSIR-National Institute of Oceanography, Goa.

### ***3.3. Mineral chemistry***

The quantitative chemical composition of selective minerals from each sub-sample was determined with an Electron Probe Micro Analyzer (EPMA, Model: Cameca SX-5) equipped with four wave length-dispersive spectrometers at CSIR-National Institute of Oceanography, Goa. Major elements (Na, Mg, Ca, Al, Ba, Sr, Si, Fe, Mn, Co Ni, Cu, Zn, Pb, and S) were analyzed on polished sections of samples by using accelerating voltage of  $\sim 15$  kV, beam current of  $\sim 12$  nA, and a beam diameter of  $2.0 \mu\text{m}$ . The standard materials including pyrite, chalcopyrite, sphalerite, and galena (from SPI Supplies, USA) were used to assess the accuracy of microprobe analyses. More than 15 spot analyses were carried out in different mineral phases in each sample.

### ***3.4. Bulk elemental composition***

For bulk chemical analysis, 20 mg of powdered sub-samples were mixed with 10ml acid mixture (HF:HNO<sub>3</sub>:HClO<sub>4</sub>:: 7:3:1) and 0.5ml saturated solution of extra-pure NaCO<sub>3</sub> and then evaporated to complete dryness. To this 20 ml (1:1) ultra pure nitric acid was added and final volume made up to 100 ml with Milli-Q water. Trace elements were analyzed with a quadrupole ICP-MS using Rh<sup>103</sup> solution (20 ng/ml) as the internal standard (Balaram and Gnaneshwar Rao, 2003) at Pondicherry University. Standard reference material, IF-G (from Groupe International de

Travail, France) was used for instrument calibration and the analytical precision with <5.0 % RSD were achieved. The composition of major elements in same solutions was analyzed by using an ICP-OES at CSIR-National Institute of Oceanography, Goa.

### ***3.5. Sulfur-isotope ratio***

Sulfur isotopic ratios ( $^{34}\text{S}/^{32}\text{S}$ ) in all sub-samples were estimated with an IRMS at CSIR-National Institute of Oceanography, Goa. For isotopic measurements, mostly monomineralic parts of each sub-sample were separated out from the bulk sample under a microscope and crushed into fine powder. The powdered samples were mixed with  $\text{V}_2\text{O}_5$  in tin capsule and then completely combusted in presence of oxygen at  $1050^\circ\text{C}$ . The gas mixture produced during combustion was swept in helium stream over combustion catalyst of tungsten oxide to produce  $\text{SO}_3$ . Available  $\text{SO}_3$  is subsequently reduced to gaseous  $\text{SO}_2$  using pure copper granules. Water vapor was removed by magnesium perchlorate moisture trap.  $\text{SO}_2$  was separated from other gas impurities by a chromatographic column (PTFE tubing) at  $100^\circ\text{C}$ . The resultant  $\text{SO}_2$  was analyzed for S-isotope ratios using an IRMS having conflo-III interface. The stable S-isotope ratios are expressed in terms of permil (‰) relative to the composition of Vienna Canon Diablo Troilite (V-CDT) and presented as:  $\delta^{34}\text{S}_{\text{V-CDT}} = [ \{ (^{34}\text{S}/^{32}\text{S}_{\text{sample}}) / (^{34}\text{S}/^{32}\text{S}_{\text{V-CDT}}) \} - 1 ] 1000$  (Coplen and Krouse, 1998). The reproducibility of  $\delta^{34}\text{S}_{\text{V-CDT}}$  values <0.29 ‰ was obtained for each sample. External calibration was prepared using IAEA standards S-1, S-2, S-3, SO-5, and SO-6.

## **4. Results**

### ***4.1. Short peripheral chimney (sample: M2255-2)***

The horizontal section of the short chimney has diverse mineral zonings with the dominance of massive anhydrite in the external rim, E2 (Table 1; Figs. 3A and 4A) and wurtzite in the inner layers, M2 and O2 (Table 1; Figs. 3C-E; 4C). X-ray diffractograms of O2 and M2 layers showed there was a minor amount of sphalerite, and traces of pyrite and chalcopyrite were also present. The wurtzite grains from the middle layer of the wall were relatively larger in size and had a composition of 56.4 - 60.9 wt% Zn; 31.3 - 32.4 wt% S and 3.9 - 4.9 wt% Fe. In contrast, the finer wurtzite grains close to fluid channel contain 60.5 – 63.4 wt% Zn, 32.5 – 33.0 wt% S and 3.9 – 5.1 wt% Fe (Table 3). Few crystals were characterized with negligible Cu (0.01 -0.2 wt%) and Ni (0.01 -0.1 wt%). The bulk elemental concentration in anhydrite-rich layer E2 also notably differs

from two inner layers. Dark inner layers, M2 and O2 showed high concentration of Zn (32.4 wt% and 37.5 wt% respectively) followed by Fe (4.1 -5.4 wt %) and Cu (1.5 -3.0 wt%). Whereas, chalcophiles are depleted in E2 (Zn =6.8 wt%; Fe =1.2 wt% and Cu =0.6 wt %) (Table 2). In contrast, elements including low ionic radii lithophiles (LILEs – Ba, Sr) and high field strength elements (HFSE –Zr, Nb, Hf) are relatively enriched in E2 layer (Table 2). S-isotope ratio also varies across this chimney section with maximum  $\delta^{34}\text{S}$  value in external E2 layer (18.76 ‰) followed by M2 ( $\delta^{34}\text{S}$  = 5.9 ‰) and O2 ( $\delta^{34}\text{S}$  = 3.4 ‰) (Table 2).

#### ***Giant central chimney (sample : M2255-10)***

Sub-samples from the vertical section of this chimney (L10, C10, and R10) have pyrite (Table 1) as major minerals with the significant amount of sphalerite and chalcopyrite. Scattered distribution of massive barite and amorphous silica (Figs. 5A and 5B) were found to be associated with sulfide minerals in lateral halves (L10 and R10) of the chimney wall. Electron microprobe analyses of minerals show chalcopyrite grains in C10 layer (Figs. 5C and 6B) has a composition of 34.4 -35.3 wt% Cu, 30.2 -31.2 wt% Fe and 28.2 -30.8 wt% S (Table 4). Besides these elements, a minor amount of Zn (<0.1 wt%) and Co (<0.05 wt%) were also occasionally recorded in some chalcopyrite crystals. The pyrite deposit has estimated composition with 44.3 - 46.2 wt% Fe and 44.3 –50.4 wt% S (Table 4). Bulk chemical composition dominates with Fe (20.5 –23.0 wt%), followed by Cu (8.9 -11.6 wt%) and Zn (1.9 -3.8 wt%). Lighter S-isotope composition ( $\delta^{34}\text{S}$  =3.8 ‰) was found in C10 as compared to lateral halves ( $\delta^{34}\text{S}$  =8.8 and 9.3 ‰) (Table 2).

#### ***4.2. Talus deposit (sample: M2255-9)***

The surface porous layer of the talus, P9 mostly contains marcasite, pyrite, and wurtzite with traces of barite and galena (Table 1). Dark bladed (20 - >50  $\mu\text{m}$ ) marcasite crystals occurred in groups (Figs. 7A and 7C) and has well-developed faces. The dendritic barite (Fig. 7D) and few Zn-sulfide crystals were mostly found as isolated growths in these marcasite clusters. The dark gray colored other three layers of talus deposit (T9, C9, and B9) contain pyrite with traces of galena, opal, and barite (Table 1). Microprobe analyses also indicate that both pyrite and marcasite in each layer were nearly pure Fe-sulfide (43.7 –48.0 wt% Fe and 47.8 –53.3 wt% S) and thus more compatible to the stoichiometric formula of  $\text{FeS}_2$ . The other trace elements had very low concentration (<0.25 wt%, Table 5). The indiscriminate growth of feather-like dendritic barite crystals in the same layer show average composition of 54.0 wt% of Ba and 8.8 wt% of S (Table

5). The bulk composition of talus showed Fe as the major constituent (20 -32 %) while elements like Cu, Zn, Ba, and Pb were reasonably low (maximum 2.2 wt%, Table 2). All four sub-samples were rich in lighter S-isotope ( $\delta^{34}\text{S} = 2.6 - 4.3 \text{ ‰}$ , Table 2).

## 5. Discussion

Analyses of sulfides from three hydrothermal structures in Vienna Woods field showed quite diverse mineral assemblages, elemental and isotopic composition; indicating different evolutionary histories. Moreover, results showed prominent mineral zonings and compositional variety within the individual deposit. Such mineral zonings and chemically discrete microenvironments are common within hydrothermal deposits and developed due to changes in evolutionary conditions during their growth (Paropkari et al., 2010; Kristall et al., 2011; Devok et al., 2016). These changes are mostly contributed by the alteration of physiochemical nature of source fluid due to change in fluid-seawater mixing ratios and/or change in temperature of precipitation (Haymon 1983; Hannington and Scott, 1988; Marchig et al., 1988; Koski et al., 1994; Paropkari et al., 2010; Kristall et al., 2011; Ray et al., 2014; 2016).

### 5.1. Evolution of small peripheral chimney (M2255-2)

This cylindrical active chimney at the edge of the vent field was characterized by 3 -4 cm thick wall and a meandering central fluid channels. The chimney wall is mostly made up with Zn-sulfide and has elevated concentration of V, Cd, Ga, and Pb; but depleted in elements like Cu and Fe. Such geochemical composition was very similar to low temperature ( $\sim 250^\circ\text{C}$  or less) immature hydrothermal chimneys reported in other oceans (Styrt et al., 1981; Paradis et al., 1988; Koski et al., 1994; Kim et al., 2004). The Zn-sulfide in this chimney was mostly present as euhedral wurtzite with less sphalerite. The abundant hexagonal wurtzite appeared as isolated or stacked composite platelets (Figs. 3C-E), had the grain size ranging between  $<10$  to  $300\mu\text{m}$  and apparently indicative of certain evolutionary conditions involve in chimney formation. Experimental observation showed that metastable wurtzite crystallizes only at the temperature  $>1020^\circ\text{C}$  from pure ZnS and at  $850^\circ\text{C}$  from Fe-rich ZnS (Kojima and Ohmoto, 1991 and references therein). Otherwise, the occurrence of crystalline wurtzite under low temperature ( $<250^\circ\text{C}$ ) condition indicates low fugacity of  $\text{H}_2\text{S}$  ( $f_{\text{S}_2}$ ) in source fluid (Scott and Barnes, 1972) and/or rapid cooling of solution supersaturated with Zn (Kojima and Ohmoto, 1991). According to the earlier study, the fluid venting from this vent field had low concentration of dissolved  $\text{H}_2\text{S}$  ( $\text{H}_2\text{S}_{\text{max.}} = 1.6 \text{ mM}$ ; Reeves et

al., 2011) and therefore, the observed mineralogy and elemental composition substantiate the low temperature formation of small peripheral chimney.

The mineral assemblages and bulk geochemistry of small peripheral chimney were completely different from the large Cu-Fe-rich central chimney, M2255-10 (Table 1). Such diversity of sulfide geochemistry in same vent field suggests, even being fed by same magma source, but the certain processes alter the nature of source fluid prior to their deposition. In smaller chimney, low concentration of Cu and Fe (as compared to M2255-10) suggests, source fluid of this chimney lost most of the Fe and Cu in the sub-surface environment. Therefore, it can be anticipated that fluid for peripheral chimneys might not venting directly from high temperature stock-work zone. Instead, sluggish fluid flows through the subsidiary branched channels likely fed those smaller chimneys and that would responsible for geochemical changes of source fluid due to conductive cooling. Such cooling effect might cause sub-surface precipitation of Fe, and Cu but allow fluid to retain elements like Zn, V, Pb, and Cd; usually remain in solution even at low temperature hydrothermal environments. This mechanism is similar to those described for the origin of low temperature Zn-rich chimneys in other studies (Koski et al., 1994). Moreover, the average Fe contents in wurtzite grains from short peripheral chimney were substantially lower ( $Fe_{max} = 5.1$  wt% in wurtzite, Table 3) than those reported in hydrothermal wurtzite from 21°N EPR (10 -20 wt% Fe; Styr et al., 1981), Endeavour (4 – 28 wt% Fe; Tivey and Dilaney, 1986) and Cleft (3 -18 wt% Fe; Koski et al., 1994) segments of Juan de Fuca Ridge. This also probably indicates the poor availability of Fe in low temperature fluid during sulfide precipitation in the peripheral chimney. Earlier studies showed more oxidizing redox condition of fluid also can develop such Fe-poor Zn-sulfides in hydrothermal system (Kawasumi and Ciba 2017; and references therein). The fluid flow through branched channels may enhance the possibility of oxidative changes of fluid and would responsible for the development of Fe-poor Zn-sulfides in peripheral chimney.

The cross section of the peripheral chimney wall had three distinct mineral zonings, which includes the anhydrite-rich porous outer layer, E2; anhydrite-sulfide-silicate mixed middle layer, M2, and Zn-sulfide dominated innermost layer, O2 (Figs. 4A -C). This mineral distribution suggests chimney development initiated with precipitation of anhydrite as the outer rim of its wall and later inward thickening of the wall took place due to deposition of metal-sulfides. Generally, hot hydrothermal fluid comes out through cracks on seafloor and thus mixing of hot Ca-rich fluid



with dissolved sulfate in ambient seawater crystallizes anhydrite at temperature  $>150^{\circ}\text{C}$  and act as initial cementing material for further growth of chimney (Haymon, 1983; Goldfarb et al., 1983; Tivey, 1998). Later, as the anhydrite wall matures, less permeable and thicker wall restricts the mixing of fluid with seawater and favor precipitation of metal sulfides around the fluid flow channel within the chimney structure (Alt et al., 1987). The polished section of middle layer M2 showed abundance of Zn-sulfides (wurtzite with less sphalerite) intergrowths of anhydrite (Fig. 4A) and silica grains (Fig. 4B). This sulfate-sulfide-silica mixed layer, M2 clearly indicates the transition phase of the chimney growth. The dispersed sulfide crystals in this mixed layer would likely form due to precipitation of  $\text{H}_2\text{S}$  rich fluid in the pore space available within anhydrite deposit, precipitated in advance. Alternatively, gradients of temperature and sulfur fugacity across the chimney wall caused partial dissolution of anhydrite and subsequent replacement with sulfide minerals could also develop such mixed layer. The euhedral to subhedral wurtzite crystals in the M2 layer are quite larger ( $>180\ \mu\text{m}$  or more). But the chimney interior (layer O2) was devoid of any anhydrite and mostly contained disseminated finer wurtzite (Fig. 4C) intergrown with amorphous silica and traces of pyrite. Thus altogether these mineral zonings across the smaller chimney wall identify two major growth phases which include early sulfate and followed by sulfide-silica phases (Fig. 10A).

Like mineralogical variation, the distinct S-isotopic compositions in three layers also indicate temporal changes in growth mechanism. The heavy isotope ratio in anhydrite of layer E2 ( $\delta^{34}\text{S} = 18.76\ \text{‰}$ ) was very close to that found in seawater sulfate ( $\delta^{34}\text{S} = +21.0\ \text{‰}$ , Rees et al., 1978), suggesting fast precipitation of  $\text{CaSO}_4$  involving ambient seawater at the initial stage of chimney growth. Compared to contemporary seawater, the slightly lighter S-isotopic ratio of sulfate-S in anhydrite layer E2 could originate either due to (1) oxidation of  $\text{H}_2\text{S}$  in hydrothermal fluid or (2) subsurface disproportionation of magmatic volatile  $\text{SO}_2$ . However, extremely low  $\text{SO}_4$  concentration (0.7- 1.8 mmole/kg; Reeves et al., 2011) in end-member fluid from Vienna Woods field possibly indicate low sulfidation environment with limited presence of gaseous  $\text{SO}_2$  or aqueous  $\text{SO}_4$  of magmatic origin. Therefore, the first mechanism involving oxidation of sulfides would be the most suitable explanation for the isotopic composition. In contrast, the isotopic values of S in wurtzite from two inner layers, M2 and O2 were quite low ( $\delta^{34}\text{S} = 5.9$  and  $3.4\ \text{‰}$  respectively). This range was quite comparable to those reported in chimney sulfides from adjacent

PACMANUS vent field ( $\delta^{34}\text{S} = 1.0$  to  $4.3$  ‰) but substantially heavier than those ( $\delta^{34}\text{S} = -8.0$  to  $-3.9$  ‰) reported in SuSu Knoll vents in the eastern Manus Basin (Kim et al., 2004). Isotopic values of layers M2 and O2 suggest precipitation of those layers took place from  $\text{H}_2\text{S}$  rich hydrothermal fluid and thus confirm the evolutionary mechanism as mentioned before. Besides mineralogy and isotopic signatures, bulk geochemistry showed concentration of Cu, Fe, and Mo progressively increase from outer to inner layers (Table 2). Such interlayer heterogeneity possibly indicates the temperature of precipitation increases as the chimney wall grows inward. But Sr, which mostly contributed by seawater and presumably concentrate in anhydrite lattice, had maximum enrichment in the outer E2 layer. With chimney maturity, thickening of chimney wall reduced the contribution of ambient seawater and responsible for gradual drops of Sr concentration in the inner M2 and O2 layers. The negative relations ( $R^2 > 0.7$ ) of bulk Sr with Cu and Fe (Figs. 9A and B) in this chimney also confirm less influence of seawater facilitated more deposition of Cu and Fe from fluid.

### ***5.2. Evolution of giant central chimney (M2255-10)***

The morphology of this, 14 m high cone-shaped chimney structure was quite similar in appearance to the large, broad-based, mature hydrothermal spires reported on the Axial Seamount (Hannington and Scott, 1988) or Southern Explorer Ridges (Scott et al., 1984). The projection of this central chimney had the maximum width of ~4cm and a well defined central fluid channel (Fig. 2C). This chimney (M2255-10) is predominantly made up with anhedral pyrite, sphalerite, and chalcopyrite. Lizitsyn et al. (1993) also reported marcasite as the major mineral in another portion of the same chimney. Concentration of Fe (20.5 – 23.0 wt%), Cu (8.9 -11.6 wt%), Mo (52 -57 ppm), Sn (4 -6 ppm) and W (3.8 -7.6 ppm) in this central chimney (Table 2) resemble typical high temperature ( $>250^\circ\text{C}$ ) hydrothermal sulfide deposits described elsewhere (Fouquet et al., 1991; Koski et al., 1994; Gena et al., 2013). The *in situ* measurement showed that vent fluid emanating through this gray smoker chimney had temperature of  $275.7^\circ\text{C}$  (Lizitsyn et al., 1993; 1997). Therefore, giant structure and sulfide geochemistry of this chimney suggests vigorous flow of hot fluid from deep stock work zone is responsible for its growth.

The distinct color variation in hand specimen (Fig. 2C) corresponds to diverse mineralogy and geochemistry at different parts of this chimney section; suggesting variable nature of fluid involved at the different growth stages. The lateral halves of chimney wall, presumably formed at the early

stage of chimney development contained more sphalerite and siliceous inclusions (Fig. 6C). However, unlike smaller chimney, there was no anhydrite mineralization has been observed. The absence of anhydrite on the external rim could be explained either by (1) dissolution over the period of time or (2) lack of anhydrite as initial cementing material. The dissolution effect cannot be ruled out because anhydrite can get dissolved in case of its exposure to fluid or fluid-seawater mixture below 180°C (Tivey and Delaney, 1986), ejecting from other active vents in the surroundings. Otherwise, the barite and silica in outer wall indicate instead of anhydrite, the growth of this large chimney initiated with silica (and barite) precipitation. A similar growth mechanism involving the precipitation of barite and silica at the beginning of chimney formation was also reported by Hannington et al. (1988). Moreover, amorphous silica in outer wall usually provides good stability for tall standing hydrothermal chimneys (Tivey and Delaney, 1986) and thus ample silica deposit (Fig. 5B) in L10 and R10 helped this chimney to grow in the large structure. Massive chalcopyrite (>50 µm) were mostly abundant in the dark central layer, C10, around the feeder channel, but the grain size sharply drops towards the outer rim of the wall (Fig. 6). The continuous flow of high temperature ( about 280°C) fluid through the central channel would develop sharp temperature gradient across the chimney wall and likely responsible for maximum occurrence chalcopyrite in C10; as compared to lateral halves (L10 and R10) of the chimney wall. A similar observation with plenty of high temperature mineral formation near fluid channel compared to edges of hydrothermal chimney wall was also noticed by Tao et al., (2011) and Gena et al., (2013).

Like mineralogy, the elemental distribution also showed substantial variability across this chimney section. Among three sections, the central C10 had the maximum abundance of Cu, Fe, Co, Mo and highest Cu/Zn ratio of 3.7; but depleted in other trace elements (e.g. Sc, Ti, V, Ni, Y, Zr, Hf, Th, and U) (Table 2). High temperature fluid flow helps to keep most of those trace elements in mobile fluid phase and thus made them least abundant in sulfide deposit. Relatively lighter S-isotopic composition ( $\delta^{34}\text{S} = 3.8 \text{ ‰}$ ) of chalcopyrite in C10 is very similar to previously reported values in large chimney of same vent field ( $\delta^{34}\text{S} = 3.0 - 5.5 \text{ ‰}$ ; Lein et al., 1993) and also comparable to high temperature sulfides over oceanic ridges ( $\delta^{34}\text{S} = 1.2 - <5.0 \text{ ‰}$ , Fig. 11). The lighter isotopic ratio around fluid channel suggests more equilibrium S-isotope fractionation between  $\text{H}_2\text{S}$  in fluid and sulfide minerals. Whereas, the isotopic composition in sulfides from L10 and R10 ( $\delta^{34}\text{S} = 9.1 \text{ ‰}$  and  $8.8 \text{ ‰}$  respectively) were rich in heavier isotopes; however, lying within

the range observed in sulfides reported from other back-arc settings (Fig. 11). Usually, heavier isotopic composition ( $\delta^{34}\text{S} > 5.0 \text{ ‰}$ ) in hydrothermal sulfides originates from sub-surface reactions involving higher seawater-rock ratios (Ohmoto et al., 1976; Styr et al., 1981). Therefore, this result probably suggests fluid at the initial phases of chimney growth has more contribution from percolated seawater. The relative enrichment of Sr in L10 and R10 (as compared to C10; Table 2) also could be due to excess inputs from seawater and confirms the hypothesis. However, the contribution from sulfate minerals (e.g. barite) available in these layers for such heavier isotopic composition cannot be ruled out completely. Thus the distribution of minerals, elements, and S-isotopic ratios has spotted out at least two distinct growth phases across this giant chimney section involving different types of source fluid. Initially, chimney development started with mixed sulfate-sulfide-silica phase originated from fluid having more seawater components and as the chimney mature, with paragenetic shift, higher temperature sulfides dominates over other minerals (Fig. 10B).

#### ***Formation of talus (M2255-9)***

The talus deposits in this vent field mostly composed of sulfide debris; probably originated from local mass wasting or broken chimney fragments (Lizitsyn et al., 1993; Gena, 2013). However, the talus (M2255-9; Fig. 2D) which collected from the base of the central chimney doesn't look a part of any chimney or spire but resembles more a piece of massive sulfide. The mineralogy and elemental composition of talus sample also differ significantly from chimney sections. Even though, it is difficult to predict the actual origin of talus; but the observed lighter S-isotopic composition in talus ( $\delta^{34}\text{S} = 2.6 - 4.3 \text{ ‰}$ , Table 2) is quite comparable to sulfides originated from magmatic materials having adequate reduced sulfur and low water-rock ratio (Zierenberg et al., 1984; Zeng et al., 2017). Thus, the possibility of disintegration of dome-shaped massive sulfide base, which would develop directly from the magmatic component, cannot be ruled out as the origin for such talus accumulation. The occurrence of crystalline marcasite (size 20 -> 50  $\mu\text{m}$ , Figs. 7A and C) as dominant Fe-sulfide suggesting sulfides in talus were likely to have formed from the Fe-rich fluid, containing sufficient amount of dissolved polysulfides. Earlier studies also showed that abundant well crystalline marcasite usually developed from Fe(II)-rich fluid, containing non-protonated polysulfides or sulfane ( $\text{H}_2\text{S}_2$  or  $\text{H}_2\text{S}_4$ ) at the temperature less than 240°C and pH below 5.0 (Murowchick and Barnes, 1986). Along with marcasite, euhedral to

subhedral pyrite crystals and colloform-silica was also found in the talus. A similar dominance of marcasite with sufficient pyrite and amorphous silica has reported in low temperature (<250°C) hydrothermal sulfide (Koski et al., 1994). The bulk chemistry of talus with low Cu, Mo, and Sn but high Pb contents (Table 2) also likely suggest typical medium to low temperature formation of this talus deposit.

Like uniform physical appearance, the hand-specimen of this talus sample also exhibits almost comparable geochemical properties in different layers. Except for minor variation in the topmost P9 layer, which was exposed to ambient seawater, the concentration of most of the elements and S-isotope ratios in other three layers (T9, C9, and B9) of the talus body were quite closer. This result suggests there was no major geochemical change in the formation of original massive sulfide structure, from which talus might have formed. However, in polished sections of T9 and B9 layers, the sulfide and sulfate minerals were found to be embedded in siliceous mass (Figs. 8A -C) and which apparently indicates late stage low temperature silica precipitation engulfed the sulfide sulfate minerals developed early.

## **5. Conclusions**

Mineralogy and geochemistry of three hydrothermal structures in Vienna Woods vent field suggest that even being the constituent part of the same hydrothermal field, the nature of source fluid responsible for their growth were certainly different from each other. Different morphology, height, mineral assemblages and paragenesis of hydrothermal chimneys also confirm different modes of evolution from fluid with different temperature and composition. Nature of mineral zonings and elemental distributions suggest central giant chimney of this field formed at the higher temperature relative to smaller peripheral chimneys. However, for both the chimneys paragenetic shifts were not represented by sharp changes but on the whole two growth regimes involving early sulfate and late sulfide phases were involved in their development. Talus was identified as disintegrated part of massive sulfide dome of hydrothermal origin. Despite different evolutionary history, on average, sulfides of this field are enriched with Zn and Fe.

## **Acknowledgments**

We are thankful to the Director, CSIR-National Institute of Oceanography, Goa for his encouragement. Dr. Paropkari is highly grateful to the Chief Scientist Prof. Alexander. P. Lizitsyn

for inviting him to participate in the cruises of *R/V Akademik Mstislav Keldysh* and providing the samples to undertake scientific investigations. Authors are grateful to Mr. Girish Prabhu and Mr. Arif Sardar for XRD and SEM-EDS analyses respectively. Thanks to Dr. J. K. Dash, Pondicherry University for ICP-MS analysis. This work was carried out under the “GEOSINK” project funded by CSIR, India. This manuscript benefited from the comments made by two anonymous reviewers. It has NIO contribution No. XXXX.

## References

- Alt J C, Lonsdale P, Haymon R, Muehlenbachs K. 1987. Hydrothermal sulfide and oxide deposits on seamounts near 21°N East Pacific Rise. *Geol Soc Am Bull*, 98: 157-168
- Auzende J M, Urabe T and Scientific party. 1996. Cruise Explores hydrothermal vents of the Manus basin. *EoS Trans AGU*, 77: 244
- Auzende J M, Ishibashi J I, Beaudoin Y, Charlou J L, Delteil J P D, Fouquet Y, Ildefonse B, Kimura H, Nishio Y, Knoery J R, Ruollan E. 2000. Extensive magmatic and hydrothermal activity documented in Manus Basin. *EoS Trans AGU*, 81: 449-453
- Balaram V. and Gnaneshwar Rao T. 2003. Rapid determination of REEs and other trace elements in geological samples by microwave acid digestion and ICP-MS. *Atom Spectros* 24: 206-212
- Binns R A. and Scott S D. 1993. Actively forming polymetallic sulfide deposit associated with felsic volcanic rocks in the Manus Basin, Papua New Guinea. *Econ Geol*, 88: 2226-2236
- Both R, Crook K, Taylor B, Brogan S, Chappell B, Frankel E, Liu L, Sinton J, Tiffin D. 1986. Hydrothermal chimneys and associated fauna in the Manus back-arc basin, Papua New Guinea. *EoS Trans AGU*, 67: 489-490
- Coplen T B and Krouse H R. 1998. Sulphur isotope data consistency improved. *Nature*, 392: 32
- Crook K A W. 1990. Preliminary Report of the 21<sup>st</sup> RV Akademik Mstislav Keldysh/ Mir cruise 1990, Manus Basin Leg (21<sup>st</sup> May – 7<sup>th</sup> June), on behalf of the Keldysh/Mir Science Team, SOPAC Cruise Report 127, p. 22
- Devok V M, Rouxel O, Kouzmanov K, Bindi L, Asael D, Fouquet Y, Etoubleau J, Burgaud G, Wälle M. 2016. Enargite-luzonite hydrothermal vents in Manus Back-Arc Basin: submarine analogous of high-sulfidation epithermal mineralization. *Chem Geol*, 438: 36-57
- Fouquet Y, Von Stackelberg U, Charlou J L, et al. 1991. Hydrothermal activity and metallogenesis in the Lau back arc basin. *Nature*, 349: 778-781.
- Goldfarb, M S, Converse, D R, Holland, H D, Edmond J M. 1983. The genesis of hot spring deposits on the East Pacific Rise. 21°N. *Econ Geol Monog*, 5, pp. 184 -197

- Gena K, Chiba H, Kase K, Nakashima K, Ishiyama D. 2013. The Tiger sulfide chimney, Yonaguni Knoll IV hydrothermal field, southern Okinawa Trough, Japan: The first reported occurrence of Pt–Cu–Fe-bearing bismuthinite and Sn-bearing chalcopyrite in an active seafloor hydrothermal system. *Res Geol*, 63: 360-370
- Gena K. 2013. Deleterious elements associated with submarine hydrothermal deposits in Manus basin, Papua New Guinea. In: *Proceedings of 7<sup>th</sup> HUON Seminar on Achieving vision 2050 through higher education, research, science & technology*. Lae, Papua New Guinea, pp. 73-80
- Hannington M D and Scott S D. 1988. Mineralogy and geochemistry of a hydrothermal silica-sulfide-sulfate spire in the caldera of Axial seamount, Juan de Fuca Ridge, *Can Mineral*, 26: 603-625
- Haymon R M. 1983. Growth history of hydrothermal black smoker chimneys. *Nature*, 301: 695-698
- Ishibashi J and Urabe T. 1995. Hydrothermal activity related to arc - back arc magmatism in the Western Pacific. In Taylor B (Ed) *Backarc Basins: tectonic and magmatism*. Plenum, New York. pp. 451-495
- Kawasumi S. and Chiba H. 2017. Redox state of seafloor hydrothermal fluids and its effect on sulfide mineralization. *Chem Geol*, 451: 25-37
- Kim J, Lee I, Lee K. 2004. S, Sr, and Pb isotopic systematics of hydrothermal chimney precipitates from the Eastern Manus Basin, western Pacific: Evaluation of magmatic contribution to hydrothermal system. *J Geophys Res*, 109, doi: 10.1029/2003JB002912.
- Kojima S. and Ohmoto H. 1991. Hydrothermal synthesis of wurtzite and sphalerite at T=350-250°C. *Min Geol*, 41: 313-327
- Koski R A, Jonasson I R, Kadko D C, Smith V K, Wong F L. 1994. Compositions and growth mechanisms and temporal relations of hydrothermal sulfide-sulfate-silica chimneys at northern Cleft segment, Juan de Fuca Ridge. *J Geophys Res*, 99: 4813-4832
- Kristall B, Nielsen D, Hannington M D, Kelley D S, Delaney J R. 2011. Chemical microenvironments within sulfide structures from the Mothra hydrothermal field: Evidence from high resolution zoning of trace elements. *Chem Geol*, 290: 12-30
- Lein AY, Ul'yanova NV, Grinenko VA, Bibikova YV, Lisitsyn AP. 1993. Mineralogical and geochemical features Manus Basin hydrothermal sulfide ores, Bismarck Sea. *Geochem Intl*, 30: 57-71
- Lizitsyn A P, Crook KAW, Bogdanov YA, et al. 1993. A hydrothermal field in the rift zone of the Manus Basin, Bismarck Sea. *Intl Geol Rev*, 35: 105-126

- Lizitsyn A P, Lukashin V N, Gordeev V V, McConachy T F, Scott S D, Shevchenko V P. 1997. Hydrological and geochemical anomalies associated with hydrothermal activity in SW Pacific marginal and back-arc basins. *Mar Geol*, 142: 7-45
- Marchig V, Rosch H, Lalou C, Brichet E, Oudin E. 1988. Mineralogical zonation and radiochronological relation in large sulfide chimney from the East Pacific Rise at 18°25'S. *Can Mineral*, 26: 541-554
- Martinez F. and Taylor B. 1996. Back-arc spreading, rifting and microplate rotation between transform faults in the Manus Basin. *Mar Geophys Res*, 18: 203-224
- Mudholkar A V. and Paropkari A L. 1999. Evolution of the basalts from three back-arc basins of southwest Pacific. *Geo-Mar Lett*, 18: 305-314
- Murowchick J B. and Barnes H L. 1986. Marcasite precipitation from hydrothermal solutions. *Geochim Cosmochim Acta*, 50: 2615-2629
- Ohmoto H, Cole D R, Mottl M J. 1976. Experimental basalt-seawater interaction: sulfur and oxygen isotope studies, *EOS Trans AGU*, 57: 342
- Paradis S, Jonasson I R, LeCheminant G M, Watkinson D H. 1988. Two zinc rich chimneys from the plume site, Southern Juan de Fuca Ridge. *Can Mineral*, 26: 637-654
- Paropkari A L, Ray D, Balaram V, SuryaPrakash L, Mirza I H, Satyanarayana M, Rao T G, Kaisary S. 2010. Formation of hydrothermal deposits at Kings Triple Junction, northern Lau back-arc basin, SW Pacific: The geochemical perspectives. *J Asian Earth Sci*, 38: 121-130
- Ray D, Kota D, Das P, SuryaPrakash L, Khedekar V D, Paropkari A L, Mudholkar A V. 2014. Microtexture and distribution of minerals in hydrothermal barite-silica chimney from the Franklin Seamount, SW Pacific: Constraints on mode of formation. *Geol Sin Acta*, 88: 801-813
- Ray D, Banerjee R., Balakrishnan S., Paropkari A L, Mukhopadhyay S. 2016. S- and Sr-isotopic compositions in barite-silica chimney from the Franklin seamount, Woodlark basin, Papua New Guinea: constraints on genesis and temporal variability of hydrothermal fluid. *Intl J Earth Sci*, doi: 10.1007/s00531-016-1381-5
- Rees C E, Jenkins W J, Monster J. 1978. The sulphur isotopic composition of ocean water sulphate. *Geochim Cosmochim Acta*, 42: 377-381
- Reeves E P, Seewald J S, Saccocia P, Bach W. et al. 2011. Geochemistry of hydrothermal fluids from the PACMANUS, Northeast Pual and Vienna Woods hydrothermal fields, Manus Basin, Papua New Guinea. *Geochim Cosmochim Acta*, 75: 1088-1123
- Scott S D and Barnes H L. 1972. Sphalerite-wurtzite equilibria and stoichiometry. *Geochim Cosmochim Acta*, 36: 1275-1295



- Scott S D, Chase R L, Barrett T J, Hannington M, Fouquet Y, Juniper S K. 1984. Tectonic framework and sulfide deposits of Southern Explorer ridge, Northeastern Pacific ocean, *EoS Trans AGU*, 65: 1111
- Sinton J M. 1997. The Manus Spreading Center near 03°22'S and the Worm Garden hydrothermal site: results of Mir-2 submersible dive 15. *Mar Geol*, 142: 207-209
- Sinton J M, Ford L L, Chappell B, McCulloch M T. 2003. Magma genesis and mantle heterogeneity in the Manus Back-arc basin, Papua New Guinea. *J Petrol*, 44: 159-195
- Smith W H F. 1993. On the accuracy of digital bathymetry data. *J Geophys Res*, 98 (B6): 9591-9603
- Styrt M M, Brackmann A J, Holland H D, Clark B C, Pisutha-Arnond V, Eldridge C S, Ohmoto, H. 1981. The mineralogy and isotopic composition of sulfur in hydrothermal sulfide/sulfate deposits on the East Pacific Rise 21°N latitude. *Earth Planet Sci Lett*, 53: 382-390
- Tamaki K and Honza E. 1991. Global tectonics and formations of marginal basins: Role of the western Pacific. *Episodes*, 14, 224-230
- Tao C H, Li H M, Huang W, Han X Q, Wu G H, Su X, Zhou N, Lin J, He Y H, Zhou J P. (2011) Mineralogical and geochemical features of sulfide chimneys from the 49°39'E hydrothermal field on the Southwest Indian Ridge and their geological inferences. *Chinese Sci Bull*, 56: 2828- 2838
- Taylor B, Crook K, Sinton J. 1994. Extensional transform zone and oblique spreading centers. *J Geophys Res*, 99: 19707–19718
- Tivey M K and Delaney J R. 1986. Growth of large sulfide structures on the Endeavour segment of the Juan de Fuca Ridge. *Earth Planet Sci Lett*, 77: 303-317.
- Tivey M K. 1998. The formation of mineral deposits at Mid-oceanic ridges. *Oceanus*, 41: 22-26.
- Tufar W. 1990. Modern hydrothermal activity, formation of complex massive sulfide deposits and associated vent communities in the Manus back-arc basin (Bismarck Sea, Papua New Guinea). *Mitteilung der Osterreichischen Geologischen Gesellschaft*, 82: 183-210
- Zeng Z, Ma Y, Chen S, Selby D, Wang X, Yin X. 2017. Sulfur and lead isotopic compositions of massive sulfides from deep-sea hydrothermal system: Implications for ore genesis and fluid circulation. *Ore Geol Rev*, 87: 155-171
- Zierenberg R A, Shank-III W C, Bischoff J F. 1984. Massive sulfide deposits at 21°N, East Pacific Rise: Chemical composition, stable isotope and phase equilibria, *Geol Soc Am Bull*, 95: 922-929

## Figure Captions

**Figure 1.** Seafloor topography of Manus Basin in the southwest Pacific Ocean. The red square shows the MIR diving site, M2255 over the northern part of Manus spreading center. Bathymetric data obtained from Smith (1993).

**Figure 2.** (A) Schematic 2D diagram of hydrothermal deposits found during MIR dive M2255, in Vienna Woods (Gothic Forest) field (modified after Crook, 1990). (B) Chimney section of peripheral chimney, M2255-2, with three sub-samples (E2, M2, and O2). (C) Vertical section of a projection of central high chimney, M2255-10 with three sections (L10, C10, and R10). (D) Sample from talus deposit on pillow basalts with four sub-samples (P9, T9, C9, and B9).

**Figure 3.** SEM images of (A) Massive anhydrite in external E2 of small peripheral chimney M2255-2, (B) the EDS results. (C-E) The layered and isolated hexagonal wurtzite crystals in orifice layer, O2 and (F) the EDS result.

**Figure 4.** Microphotographs (obtained from EPMA) of polished sections from the short chimney, M2255-2. (A) Wurtzite crystals (light gray) embedded in massive anhydrite (dark gray) deposits in the outer E2 layer. (B) Hexagonal and anhedral wurtzite in siliceous deposit and (C) Wurtzite dominated innermost O2 layer.

**Figure 5:** SEM image and corresponding EDS results of the sample from the central giant chimney (M2255-10a) (A) Massive barite (white) in lateral half L10, (B) Colloform silica in L10; (C) massive chalcopyrite in C10 and (D) The EDS result.

**Figure 6:** Microphotograph (obtained from EPMA) of polished sections from the central chimney, M2255-10. (A) anhedral to subhedral pyrite and chalcopyrite deposits embedded in silicate of R10 section. (B) Large anhedral chalcopyrite deposits in C10 and (C) Chalcopyrite with sphalerite intrusion in L10.

**Figure 7:** SEM image and corresponding EDS results of the sample from the Talus deposit (M2255-9). (A) The dense accumulation of marcasite crystals in the P9 layer. (B) The EDS result. (C) Isolated barite crystal within marcasite. (D) Radiated growth of barite crystals within marcasite deposit in the C9 layer.

**Figure 8:** Microphotograph (obtained from EPMA) of the polished section from (A) top T9 shows cubic pyrite embedded in silicate deposit. (B) The bottom section B9 of the Talus, M2255-9 reveals radiated dendritic barite and anhedral pyrite surrounded by opaline silica and (C) The C9 layer having massive pyrite growths.

**Figure 9:** Plots of bulk Sr contents against concentrations of (A) Cu and (B) Fe in different sub-samples of the small peripheral chimney and central giant chimney.

**Figure 10:** Distribution of minerals representing their possible paragenetic sequences across the (A) short peripheral chimney and (B) central giant chimney.

**Figure 11:** Comparison of  $\delta^{34}\text{S}$  values of hydrothermal sulfides from Vienna Woods fields with other known sulfide deposits from various Mid-oceanic ridges and Back-arc settings. This figure is modified after Kim et al., (2004) with additional data from Devok et al., (2016) and Zeng et al., (2017).

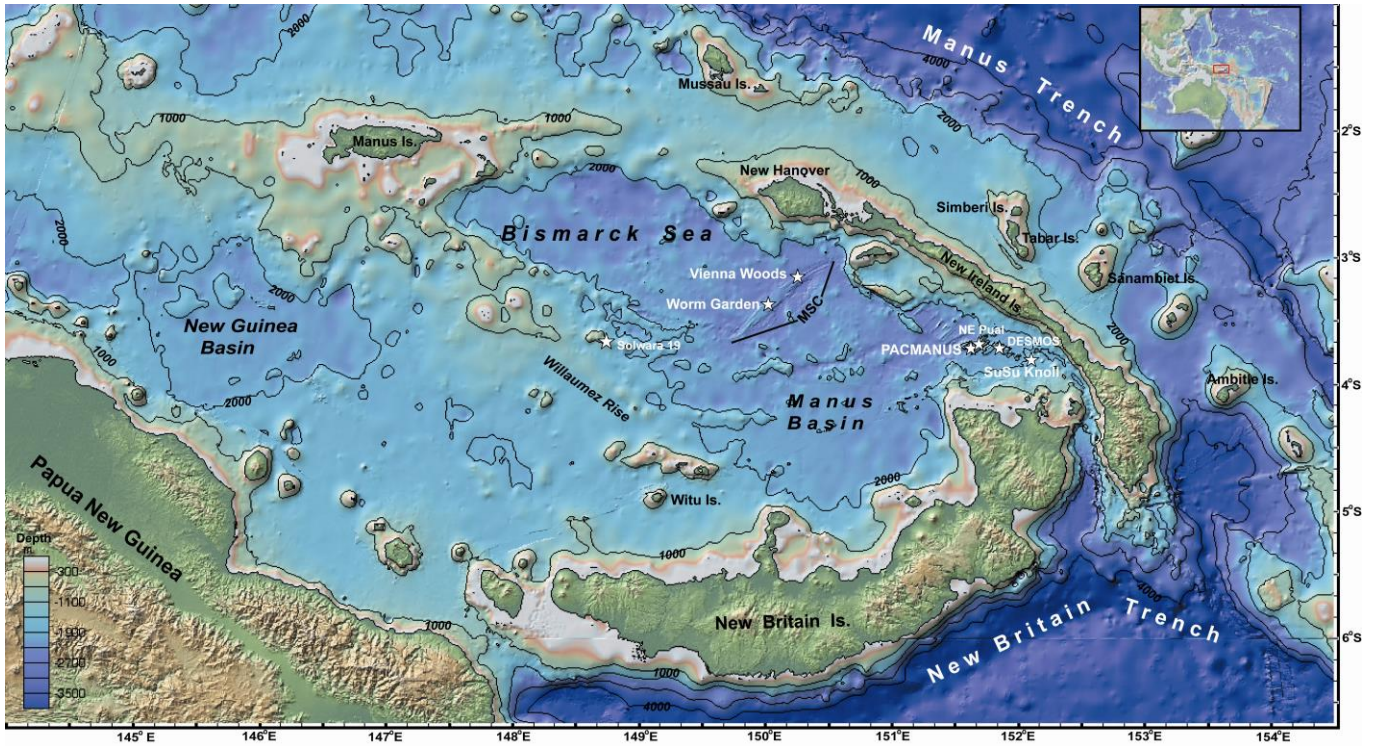


Figure 1.

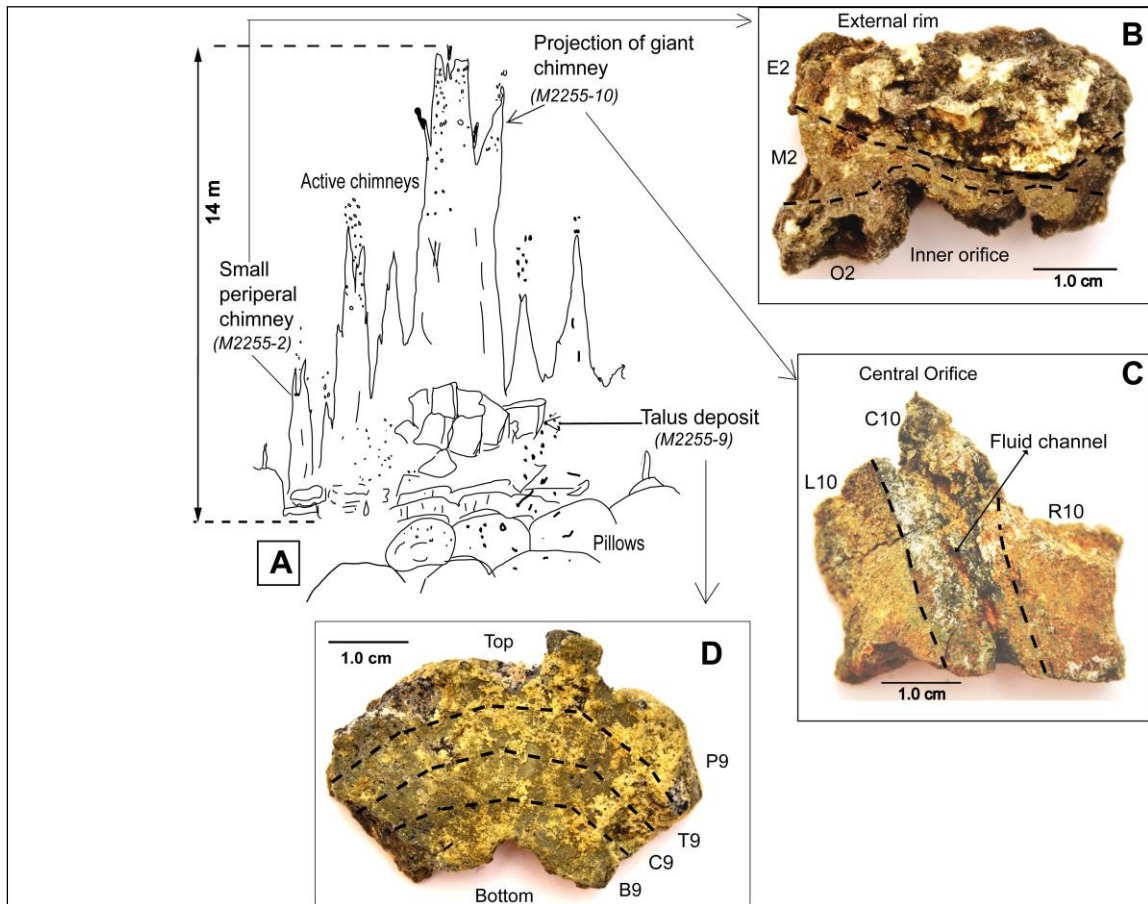


Figure 2.

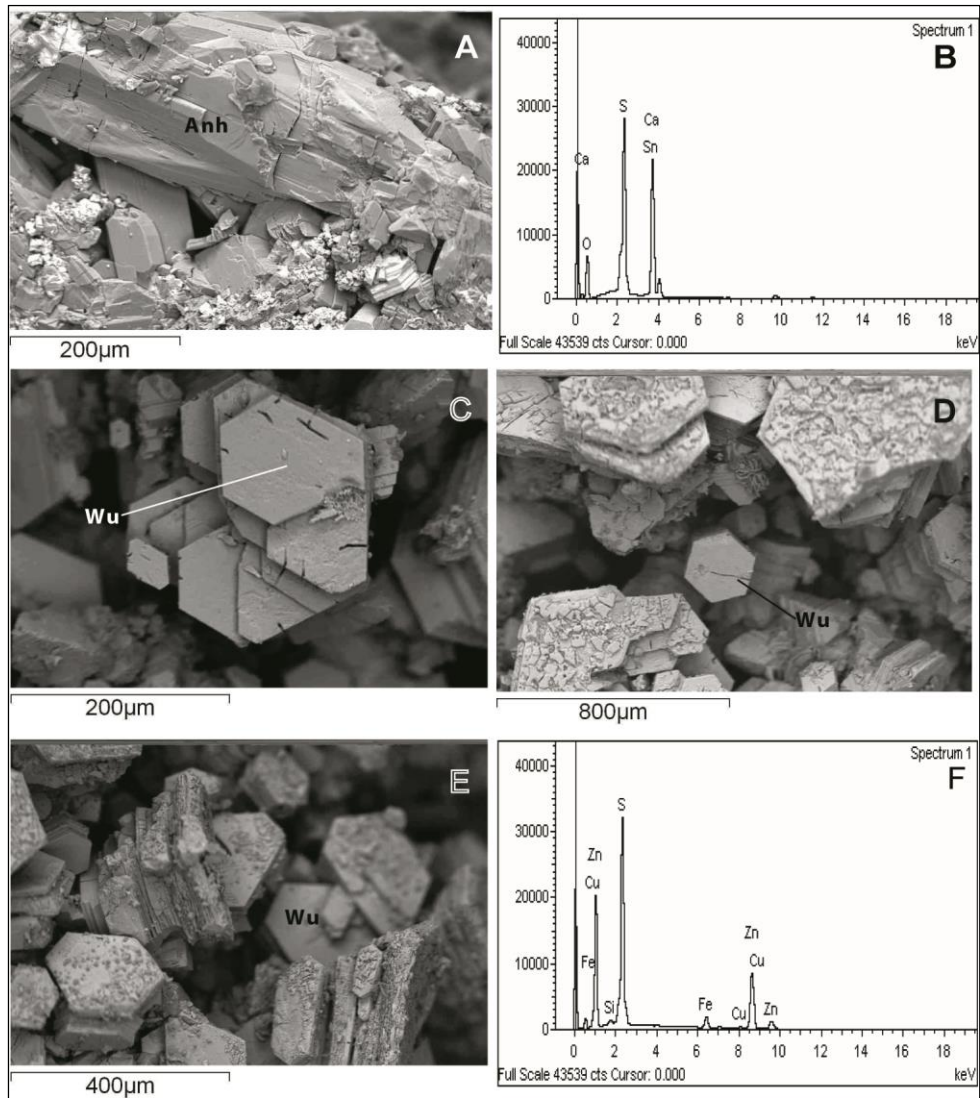


Figure 3.

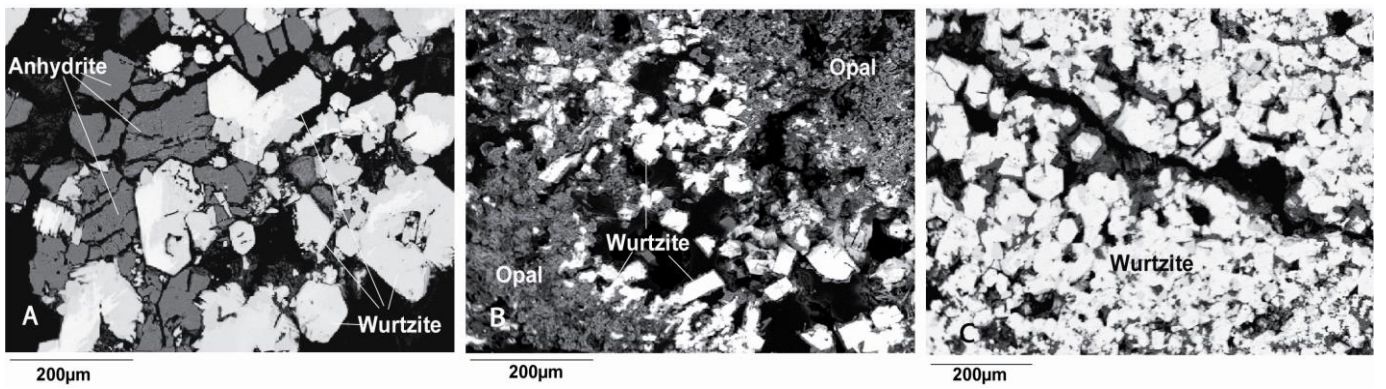


Figure 4.

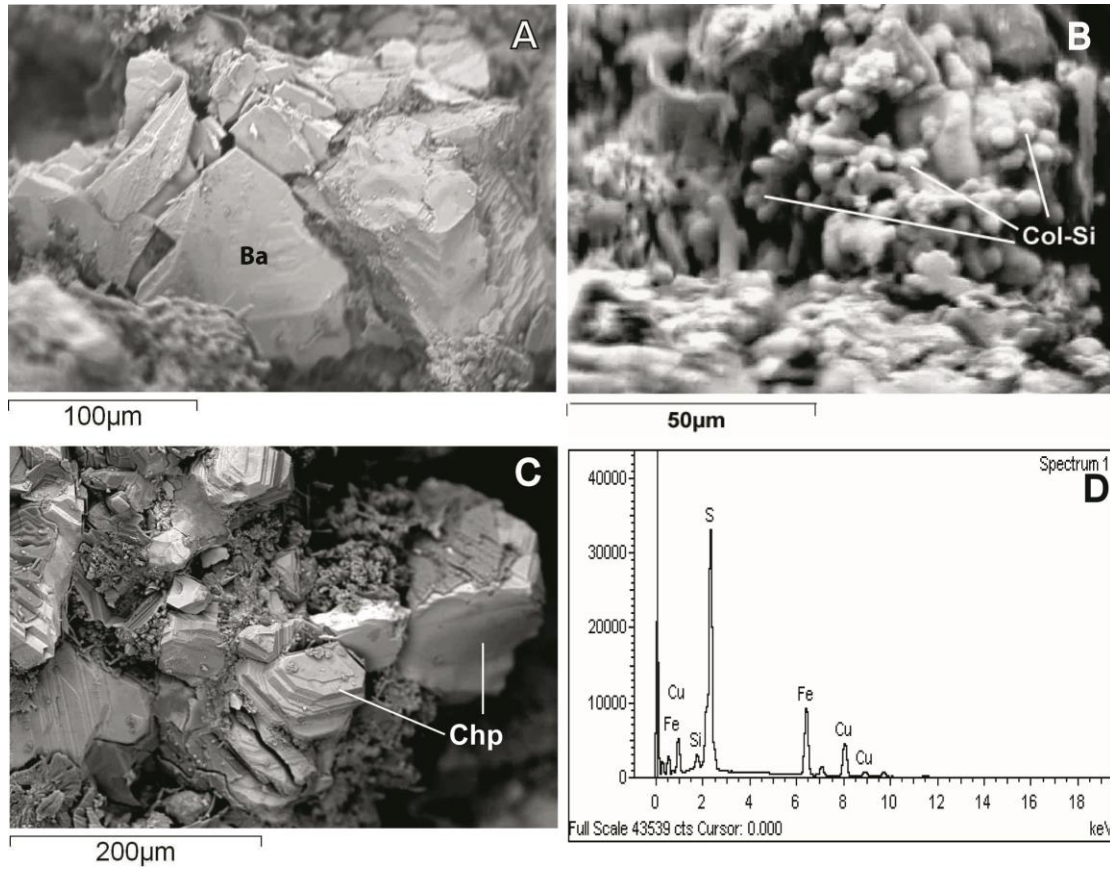


Figure 5.

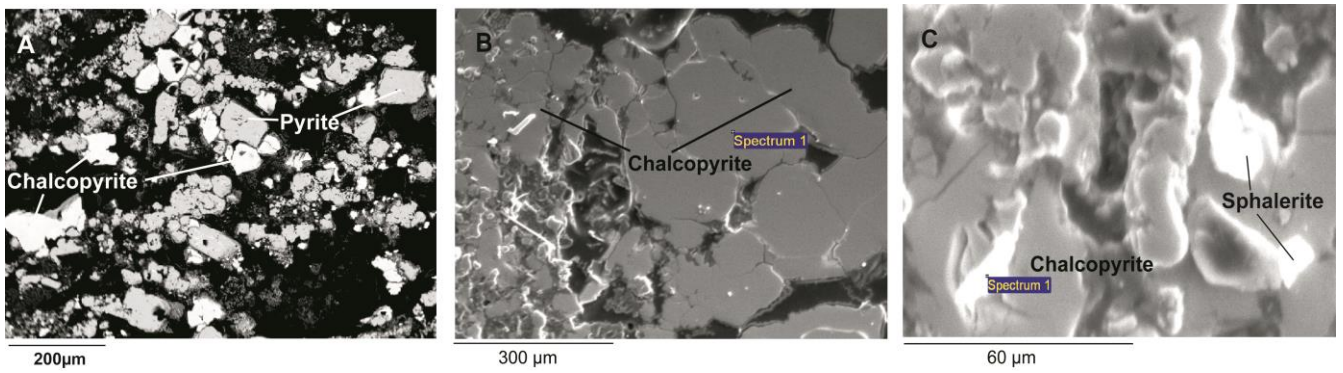


Figure 6.

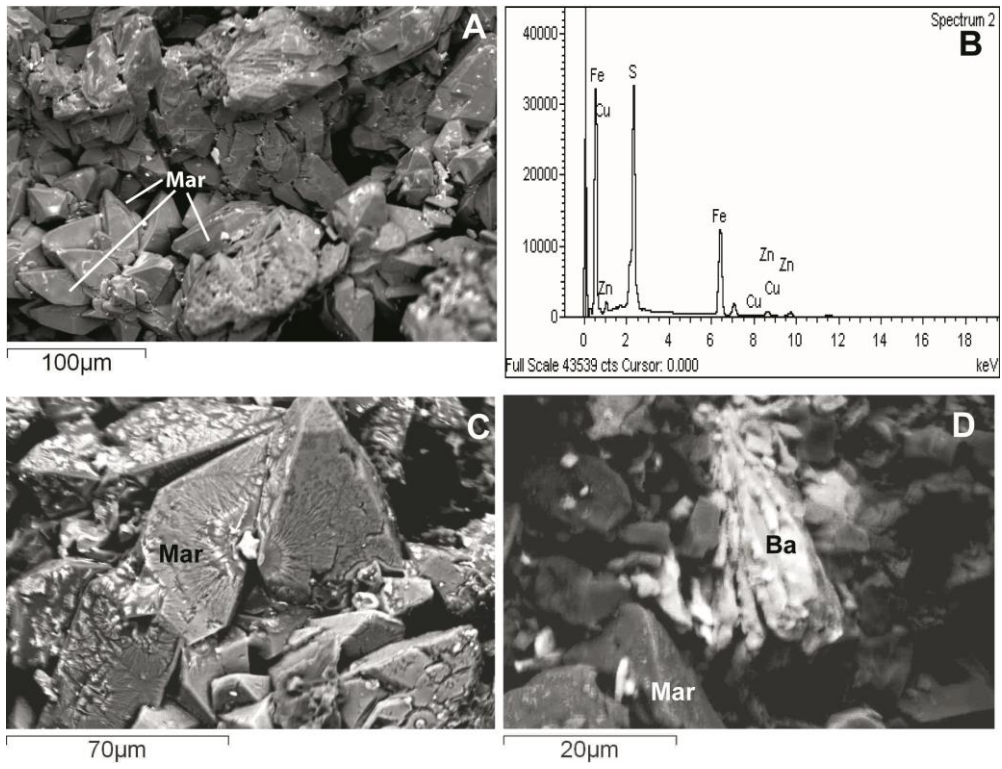


Figure 7.

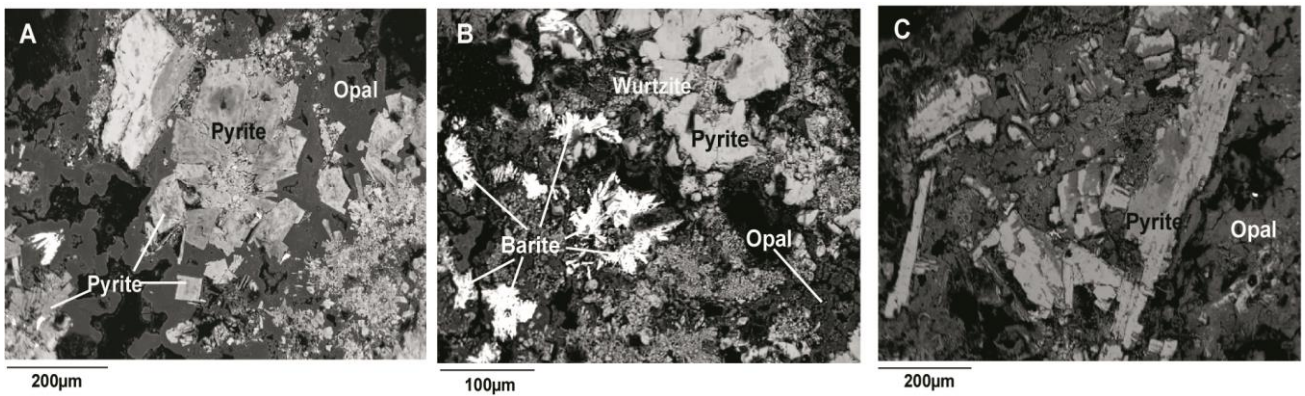


Figure 8.

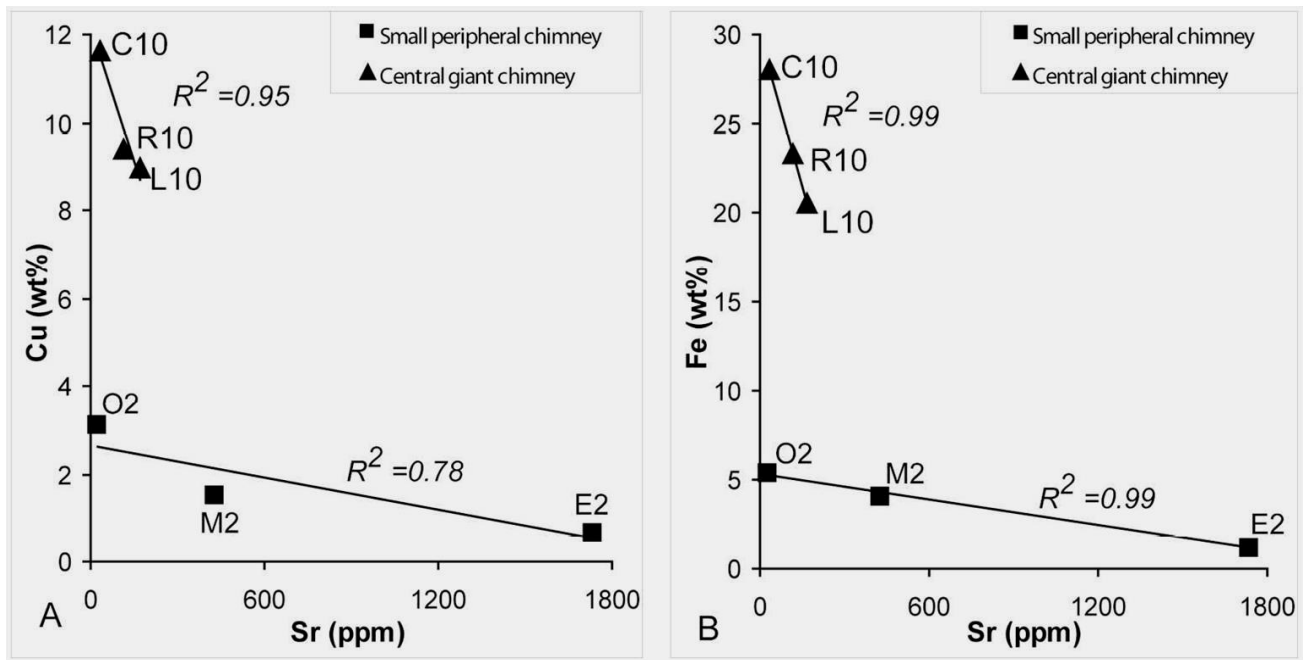


Figure 9.

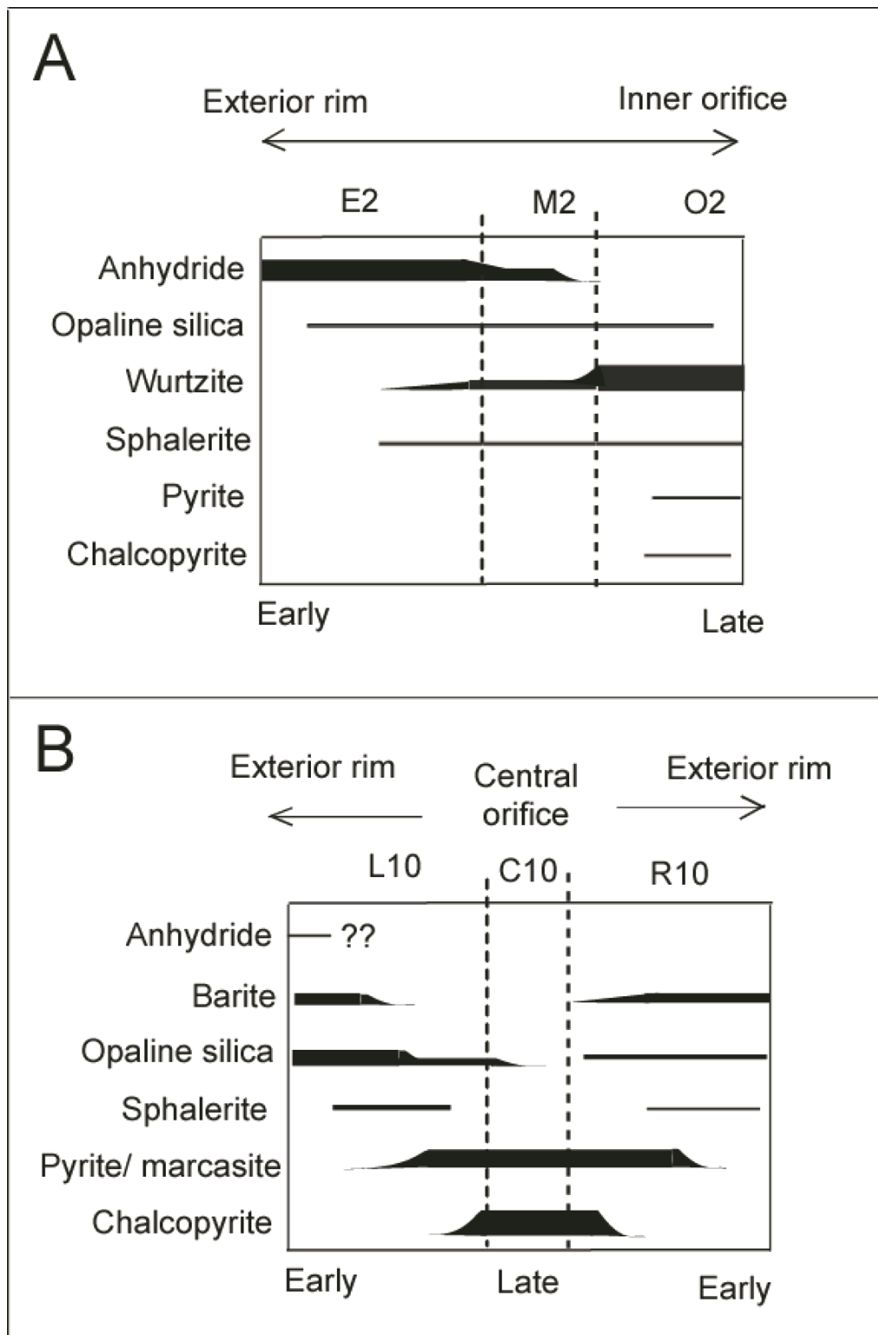


Figure 10.



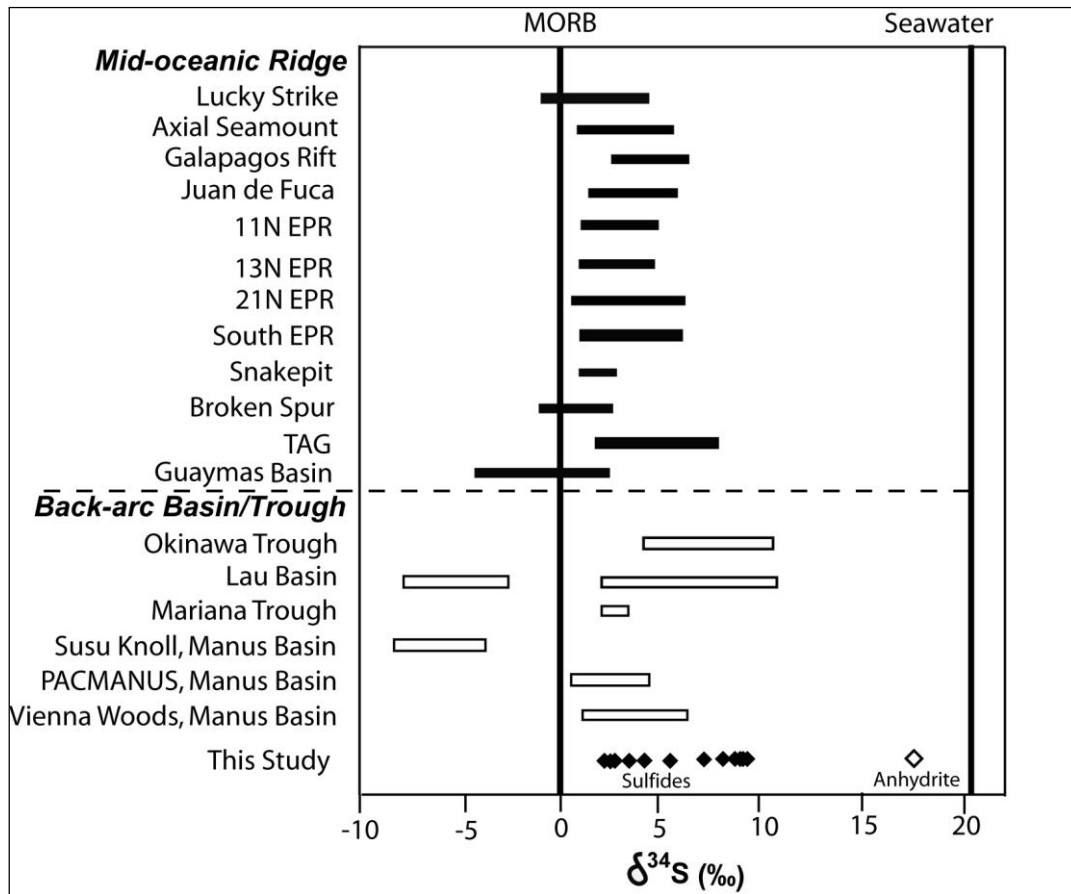


Figure 11.

**Table 1.** Minerals identified in sub-samples of chimney sections and talus deposit from Vienna Woods hydrothermal field in northern Manus spreading center.

Samples	Location (Depth)	Sub-samples	Minerals	
			Major	Minor/Trace
Horizontal section of peripheral chimney (M2255-2)	03°09.73'S 150°16.85'E (2485m)	E2	Anh	Op-Si
		M2	Anh, Wu	Py, Wu, Sph,
		O2	Wu	Py, Op-Si, Sph, Cp
Vertical section of main chimney (M2255-10a)	03°09.77'S 150°16.85'E (2485m)	L10, R10	Py, Sph, Cp	Ba, Op-Si
		C10	Cp, Py	Sph
Vertical section of Talus deposit (M-2255-9)	03°09.73'S 150°16.85'E (2500m)	P9	Mar	Py, Ba, Gal
		T9, C9, B9	Py, Mar, Op-Si	Wu, Ba, Gal

*Note:* Cp = Chalcopyrite; Op-Si = Opaline silica; Py = Pyrite; Sph = Sphalerite; Ba = Barite; Anh = Anhydrite; Wu = Wurtzite; Mar = Marcasite; Gal = Galena.

**Table 2.** Major and trace element compositions and sulfur isotopic ratios in sub-samples from different chimney sections and talus deposits from Vienna Woods hydrothermal fields in northern Manus spreading center.

Element	Horizontal section of short peripheral chimney (M2255-2)			Vertical section of large central chimney (M2255-10a)			Vertical section of talus deposit (M2255-9)			
	Exterior rim (E2)	Middle section (M2)	Orifice section (O2)	Left section (L10)	Central fluid channel (C10)	Right section (R10)	Porous surface layer (P9)	Top layer (T9)	Central layer (C9)	Bottom layer (B9)
(In wt%)										
<b>Al</b>	0.03	0.01	0.05	0.08	0.10	0.10	0.12	0.16	0.22	0.51
<b>Mn</b>	0.01	0.04	0.04	0.02	0.02	0.05	0.05	0.05	0.05	0.07
<b>Fe</b>	1.23	4.12	5.42	20.58	21.98	23.20	20.31	32.01	30.20	27.12
<b>Cu</b>	0.66	1.48	3.11	8.94	11.65	9.40	0.59	0.16	0.12	0.08
<b>Zn</b>	6.78	32.45	37.56	9.89	3.14	6.85	2.29	0.63	0.54	0.36
<b>Ba</b>	0.06	0.05	0.03	1.24	0.44	1.0	1.10	0.25	0.20	1.02
(In ppm)										
<b>Sc</b>	7.3	8.72	9.28	15.73	10.60	16.19	13.07	15.97	20.01	26.32
<b>Ti</b>	84.7	40.4	46.2	136.1	79.91	138.7	111.1	146.3	165.1	214.2
<b>V</b>	165.5	213.6	177.6	114.8	63.76	81.15	63.88	65.48	68.76	64.78
<b>Co</b>	3.07	0.05	7.09	19.75	29.05	17.96	30.02	31.57	28.95	27.40
<b>Ni</b>	5.36	1.92	1.13	3.41	1.22	1.49	26.35	3.35	3.74	3.63
<b>Ga</b>	22.3	20.8	32.5	10.1	8.5	13.2	9.6	9.8	8.1	4.7
<b>Ge</b>	5.48	8.36	9.58	25.62	15.74	17.66	18.51	20.58	21.97	21.03
<b>Rb</b>	0.72	0.60	0.98	7.04	4.07	4.22	5.21	5.12	5.73	8.46
<b>Sr</b>	1734	428.9	24.1	167	31.03	116.1	747.2	129.9	88.93	174.5
<b>Y</b>	0.24	0.13	0.15	0.25	0.18	0.27	0.25	0.30	0.25	0.32
<b>Zr</b>	2.04	0.81	0.93	5.31	3.35	6.98	5.4	6.04	5.77	6.41
<b>Nb</b>	0.33	0.17	0.17	2.74	1.22	1.19	0.56	0.97	0.76	0.69
<b>Mo</b>	7.54	16.56	24.53	57.32	77.34	52.20	11.01	26.97	30.94	37.15
<b>Cd</b>	269	1571	1732	82.5	55.64	81.0	16.41	3.44	2.99	2.58
<b>Sn</b>	0.63	3.12	0.66	6.18	4.23	5.69	0.97	0.77	0.62	0.62
<b>Hf</b>	0.16	0.02	0.03	0.15	0.11	0.19	0.17	0.16	0.15	0.17
<b>Ta</b>	3.83	0.61	1.04	134.7	49.95	41.75	14.36	30.27	23.20	17.68
<b>W</b>	1.02	0.33	0.43	7.65	3.99	3.83	0.23	3.02	2.74	2.54
<b>Hg</b>	3.48	2.37	2.79	2.64	2.76	2.40	4.5	4.09	3.51	4.32
<b>Pb</b>	262	230	331	46	90	181	4010	7630	9270	6810
<b>Th</b>	0.19	0.03	0.05	0.15	0.06	0.10	0.1	0.07	0.08	0.08
<b>U</b>	0.11	0.10	0.09	0.32	0.29	0.35	0.21	0.16	0.17	0.33
<b>Cu/Zn</b>	0.09	0.045	0.083	0.904	3.71	1.37	0.25	0.25	0.22	0.22
<b>Ba/Nb</b>	1818	2941	1764	4525	3606	840	19642	2577	2631	14782
<b>δ<sup>34</sup>S (‰)</b> (Mineral)	18.76 (Anh)	5.92 (Wu)	3.41 (Wu)	9.19 (Cp-Py)	3.87 (Cp)	8.82 (Cp-Py)	4.22 (Mar)	2.62 (Py)	2.63 (Py)	2.94 (Py)

**Table 3:** Elemental compositions (in wt. %) of anhydrite and wurtzite from E2 and O2 layers of hydrothermal chimney sample, M2255-2 respectively.

<b>Anhydrite in E2 layer</b>									
<b>Si</b>	<b>S</b>	<b>Fe</b>	<b>Cu</b>	<b>Zn</b>	<b>Ca</b>	<b>Sr</b>	<b>Ba</b>	<b>O</b>	<b>Total</b>
0.01	14.12	0.02	bdl	0.25	26.61	23.90	5.62	24.73	95.26
0.03	14.57	0.06	0.06	0.37	26.18	21.71	6.38	25.12	94.48
0.03	14.50	0.12	0.04	0.17	26.41	18.90	10.10	25.10	95.27
0.03	14.08	0.02	bdl	0.23	26.34	21.67	8.67	24.59	95.63
<b>Wurtzite in O2 layer</b>									
<b>Na</b>	<b>Al</b>	<b>Si</b>	<b>S</b>	<b>Fe</b>	<b>Co</b>	<b>Ni</b>	<b>Cu</b>	<b>Zn</b>	<b>Total</b>
1.63	0.01	0.01	32.49	5.12	0.03	bdl	0.35	61.53	101.10
1.54	0.01	0.01	31.42	4.87	bdl	0.03	0.10	60.90	98.88
1.69	bdl	bdl	32.13	4.62	0.08	bdl	0.09	60.86	99.47
1.57	0.06	0.02	32.32	4.31	bdl	bdl	0.06	60.70	99.04
1.40	0.08	bdl	32.53	4.97	bdl	0.04	0.15	60.70	99.86
1.61	0.08	bdl	32.49	4.41	bdl	0.04	0.02	62.12	100.70

\* (bdl =below detection limit) \* For elements selected for analyses, the bdl is 0.01 wt%

**Table 4:** Elemental compositions (in wt. %) of chalcopyrite and pyrite in large hydrothermal chimney sample, M2255-10.

<b>Chalcopyrite in C10 layer</b>									
<b>Na</b>	<b>Al</b>	<b>Si</b>	<b>S</b>	<b>Fe</b>	<b>Co</b>	<b>Ni</b>	<b>Cu</b>	<b>Zn</b>	<b>Total</b>
0.05	0.01	bdl	30.16	30.52	0.06	bdl	34.4	0.04	95.24
bdl	bdl	0.03	30.86	31.26	0.02	0.01	34.54	0.06	96.78
bdl	bdl	bdl	29.85	30.90	bdl	0.04	35.29	0.06	96.14
bdl	0.09	bdl	29.28	30.27	0.01	0.03	35.48	0.07	95.23
0.07	0.04	0.03	32.24	31.65	0.02	bdl	35.61	0.17	99.83
<b>Pyrite in L10 layer</b>									
<b>Na</b>	<b>Al</b>	<b>Si</b>	<b>S</b>	<b>Fe</b>	<b>Co</b>	<b>Ni</b>	<b>Cu</b>	<b>Zn</b>	<b>Total</b>
0.01	0.02	0.01	48.95	44.99	bdl	bdl	0.13	0.53	94.64
bdl	0.09	bdl	50.43	46.17	0.06	bdl	0.03	0.29	97.36
0.14	0.26	0.01	48.64	44.35	0.01	bdl	0.35	0.24	94.00
0.03	1.70	0.01	44.06	43.99	0.02	bdl	0.35	0.70	90.86
0.04	0.05	0.02	48.34	45.92	bdl	bdl	0.12	0.07	94.56

\* bdl = below detection limit. \* For elements selected for analyses, the bdl is 0.01 wt%

**Table 5:** Elemental compositions (in wt. %) of pyrite and barite from T9 and B9 layers of hydrothermal chimney sample, M2255-9 respectively.

<b>Marcasite from T9 layer</b>												
<b>Na</b>	<b>Al</b>	<b>Si</b>	<b>S</b>	<b>Fe</b>	<b>Co</b>	<b>Ni</b>	<b>Cu</b>	<b>Zn</b>	<b>Total</b>			
bdl	0.01	bdl	51.17	46.90	bdl	0.08	0.07	bdl	98.23			
bdl	0.02	0.02	50.98	47.37	0.02	0.01	0.04	bdl.	98.46			
0.04	0.18	0.01	50.22	45.28	bdl	0.06	0.06	0.16	95.97			
bdl	0.21	0.02	47.81	47.05	0.01	0.03	0.06	0.04	95.23			
0.03	0.20	bdl	49.52	46.03	0.02	0.01	bdl	0.01	95.79			
0.01	0.14	0.02	49.02	46.61	0.02	bdl	0.10	bdl	95.91			
<b>Marcasite from B9 and C9 layers</b>												
<b>Na</b>	<b>Al</b>	<b>Si</b>	<b>S</b>	<b>Fe</b>	<b>Co</b>	<b>Ni</b>	<b>Cu</b>	<b>Zn</b>	<b>Ca</b>	<b>Ba</b>	<b>Total</b>	
0.02	bdl	0.07	52.06	47.95	0.02	0.03	0.07	0.04	bdl	0.08	100.30	
bdl	0.16	0.01	50.96	46.83	0.03	0.05	0.06	bdl	0.01	0.04	98.15	
0.02	bdl	0.01	51.09	47.54	0.02	bdl	0.10	bdl	0.01	bdl	98.79	
bdl	0.02	0.01	50.51	46.13	0.13	bdl	0.25	bdl	0.03	0.05	97.13	
0.03	bdl	0.02	50.93	47.45	0.02	bdl	0.01	0.08	0.01	bdl	98.53	
0.02	0.07	0.01	53.39	48.04	bdl	0.01	0.10	bdl	0.01	0.03	101.60	
<b>Barite from B9 layer</b>												
<b>Na</b>	<b>Al</b>	<b>Si</b>	<b>S</b>	<b>Fe</b>	<b>Co</b>	<b>Ni</b>	<b>Zn</b>	<b>Sr</b>	<b>Ca</b>	<b>Ba</b>	<b>O</b>	<b>Total</b>
0.02	0.12	0.01	9.07	0.98	0.07	bdl	0.05	9.16	0.18	55.7	16.03	91.31
0.05	0.12	0.02	8.93	0.57	0.04	bdl	0.17	12.05	0.05	56.60	15.87	94.45
0.05	0.30	3.14	8.46	0.4	0.05	0.07	bdl	16.76	0.01	51.86	18.47	99.47
0.06	0.31	1.98	9.36	0.48	0.03	0.02	0.03	17.21	0.04	53.93	18.12	101.60

\* (bdl =below detection limit) \* For elements selected for analyses, the bdl is 0.01 wt%